CGI2024 manuscript No.
(will be inserted by the editor)

Dual-Mechanism Surface Tension Model for SPH-Based Simulation

Anonymous

Fig. 1: Bubble coalescence

Abstract We present an innovative Lagrangian dual-mechanism model for simulating surface tension, specifically designed to replicate the intricate interplay of liquids with textured solid surfaces and the emergence of gas bubbles. This model synergistically merges the influence of inter-particle dynamics with global surface curvature, ensuring a harmonious balance between the intricacies of fluid motion and the imperative of surface area reduction. A cornerstone of our methodology is the incorporation of Laplace pressure differentials across fluid boundaries, enhancing interface stability and enabling the depiction of distinctive droplet oscillations driven by fluctuations in kinetic energy. Additionally, our model introduces a dual-scale smoothing kernel, meticulously engineered to resolve the subtle nuances of surface textures. The prowess of our model is exemplified in its ability to simulate superhydrophobic behaviors, underscoring its utility. Integrated within the Smoothed Particle Hydrodynamics (SPH) framework, our model offers efficient simulation performance, contributing a valuable tool to the field of fluid simulation.

Keywords surface tension · Laplace pressure · rough surface · interface stability

1 Introduction

In nature, surface tension significantly influences fluid phenomena such as dropletss [12], thin-film bubbles [28, 19], and splash crowns [1,8]. The interaction of fluids with solid surfaces introduces complex behaviors like wetting and non-wetting [33,7], influenced by the surface characteristics of the materials involved. This has spurred research in Computer Graphics to accurately simulate these effects for improved visual realism.

Surface tension results from the unequal forces among molecules, modeled effectively in Smoothed Particle Hydrodynamics (SPH) [22]. SPH uses macro Lagrangian particles to simulate these molecular interactions, providing a framework for capturing fluid dynamics. Techniques such as the Inter-particle Interaction Force (IIF) within SPH address cohesion through a blend of attractive and repulsive forces. However, challenges like particle clustering and the need for larger computational resources can compromise the stability and smoothness of simulations.

To enhance simulation fidelity, the Continuum Surface Force (CSF) model [5] calculates surface tension through curvature. Yet, the CSF model struggles with accurately determining curvature near free surfaces due to kernel truncation, leading to errors and computational inefficiency [22,35,38]. These challenges underscore the ongoing need for advanced methods to simulate surface tension effectively within the confines of computer graphics research.

Furthermore, existing surface tension models have predominantly focused on fluid movement over smooth and continuous surfaces, limiting their ability to simulate specific hydrophilic or hydrophobic effects and notably failing to capture superhydrophobic behavior on rough surfaces. In real-world scenarios, contact surfaces often exhibit visible protrusions, indentations, or gaps,

particularly pronounced at smaller scales. Regrettably, traditional models, reliant on larger-scale smoothing kernels [33], tend to overlook these intricate surface details.

To overcome these limitations, we introduce a dual-mechanism surface tension model in this paper, which integrates particle interaction forces with curvature forces. Our approach differentiates between the dynamics of particles at the fluid surface and those within the bulk, while also addressing the issue of kernel truncation. Additionally, we incorporate a Laplace pressure adjustment based on the Young-Laplace equation to enhance the stability of fluid interfaces, facilitating the simulation of diverse surface tension phenomena and ensuring the minimization of surface area. A novel dual-scale smoothing kernel is proposed to recover the details lost at fluid-solid interfaces, enabling the successful simulation of Cassie [6] and Wenzel [31] phenomena, which represent two distinct states of fluid superhydrophobicity on various rough surfaces.

Our main contributions are as follows:

- Introduction of an accurate surface detection mechanism that identifies and corrects the truncated kernels of surface particles.
- Implementation of a Laplace pressure adjustment to enhance the interface stability of surface tension.
- Development of a dual-scale smoothing kernel designed to capture superhydrophobic phenomena by preserving detail on rough and discontinuous surfaces.

2 Related Work

2.1 Particle-Based Methods

Inter-particle Interaction Force Surface tension is a consequence of intermolecular interactions at the microscopic level. Several studies have approximated these interactions by introducing attractive forces between neighboring particles [9,3,33,34]. Clavet *et al.* [9] and Becker *et al.* [3] incorporated IIF within the SPH framework. Akinci *et al.* [1] and Huber *et al.* [14] combined cohesion and curvature forces to model surface tension. Despite their efforts, challenges remain, especially in simulating large surface tensions, leading to particle clustering and cobweb-like structures. Wang *et al.* [29] addressed these issues by employing Implicit Incompressible SPH (IISPH) [16]. Yang *et al.* [33,34] improved performance by using a larger smoothing kernel radius, though at the cost of increased computational complexity. Jeske *et al.* [19] proposed an implicit cohesion force to enhance surface tension stability but observed abnormal curvature at bubble adhesion surfaces.

Continuum Surface Force Another approach to model surface tension in particle-based methods is throu-gh curvature, using the CSF method [5,22,35,1,38]. Brackbill *et al.* [5] conceptualized surface tension as a volumetric force across interfaces. Morris *et al.* [21] and Muller *et al.* [22] simplified CSF for SPH. Akinci *et al.* [1] achieved results comparable to IIF with proper tuning. However, CSF faces challenges in surface detection due to noisy kernel gradient normalization and curvature estimation sensitivity to sampling. Zorilla *et al.* [38] applied a method inspired by Monte Carlo integration for estimating local normals and curvatures. He *et al.* [12] took inspiration from the Cahn-Hilliard equation to derive a similar force for handling surface tension and air pressure.

2.2 Mesh-Based Methods

Mesh-based methods diverge from particle-based techniques by focusing on tracking the fluid surface to capture finer details. Zhang *et al.* [36] introduced a deformable surface mesh for droplets. Da *et al.* [11] developed a surface-only technique using triangle meshes for surface tension simulations. Zhu *et al.* [37] utilized non-manifold simplicial complexes for thin sheets and filaments. These methods find extensive application in simulating foam, bubbles, films [10,18,17], and viscous sheets or threads [2,4].

2.3 Hybrid Methods

Hybrid methods combine Lagrangian particles and Eulerian grids to leverage the strengths of both approaches. Wang *et al.* [27] built on Zhu *et al.*'s work [37] in a Eulerian-Lagrangian framework, using transition operators for fluid volume, sheet, and filament evolution. Hyde *et al.* [15] simulated liquid metals with high surface energy using Material Point Method (MPM) and Particle-In-Cell (PIC). Chen *et al.* [7] introduced a MPM approach for Marangoni effects simulation due to tension gradients. Ruan *et al.* [25] developed a simplicial mesh membrane for strong surface tension-driven solid-fluid coupling. Xing *et al.* [32] proposed a novel Position-based Dynamics (PBD) framework approach with a local mesh structure for surface tension simulation.

We introduce a new particle-based surface tension model that combines the effects of particle interactions and surface curvature. By utilizing this dual-mechanism approach, we are able to consider both the intricacies of fluid motion and surface area minimization. The previously existing issue of estimation error in curvature

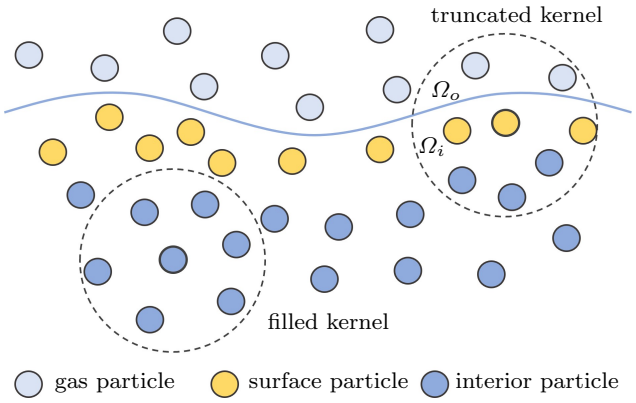

Fig. 2: Truncated kernel of surface particle.

is alleviated by incorporating Laplace pressure to correct the truncated surface particles. Furthermore, we introduce a dual-scale smoothing kernel to account for interactions between the fluid and rough solid surfaces that was previously overlooked.

3 SPH Discretization

SPH is a Lagrangian framework used for simulating fluids by discretizing them into particles [22]. Each particle represents a portion of the fluid and carries properties such as mass, position, and velocity. The Navier-Stokes equations govern the motion of fluids and in the SPH context, they are expressed as follows for particle i:

$$\rho_i \frac{D\boldsymbol{v}_i}{Dt} = -\nabla p_i + \rho_i \nu \nabla^2 \boldsymbol{v}_i + \rho_i \boldsymbol{g} + \boldsymbol{F}_i^{ST}, \tag{1}$$

where ρ_i is the density, $\boldsymbol{v}_i$ is the velocity, p_i is the pressure, ν is the kinematic viscosity coefficient, $\boldsymbol{g}$ is the gravitational acceleration, and $\boldsymbol{F}_i^{ST}$ represents surface tension forces acting on particle i.

In SPH, any scalar field ψ at the position $\boldsymbol{x}_i$ of particle i is interpolated using contributions from all particles within a certain radius (defined by the smoothing length h), as given by:

$$\psi(\boldsymbol{x}_i) = \sum_j m_j \frac{\psi_j}{\rho_j} W\left(\boldsymbol{x}_i - \boldsymbol{x}_j, h\right), \tag{2}$$

where m_j is the mass and ψ_j/ρ_j is the value of the field per unit mass for particle j. W is the smoothing kernel function, which is often chosen to be a cubic spline as suggested by Monaghan [20] for its good balance between computational efficiency and accuracy.

The pressure for each particle is computed using the Tait equation [3], a common equation of state for SPH simulations of incompressible fluids, as follows:

$$p_i = B\left[\left(\frac{\rho_i}{\rho_0}\right)^7 - 1\right], \tag{3}$$

where B is a stiffness coefficient related to the speed of sound in the fluid [23] and index is typically set to 7 for water-like fluids. ρ_0 is the rest density of the fluid.

Pressure forces are then calculated to ensure fluid incompressibility and are given by:

$$-\frac{1}{\rho_i}\nabla p_i = -\sum_j m_j \left(\frac{p_i}{\rho_i^2} + \frac{p_j}{\rho_j^2}\right) \nabla W_{ij}, \tag{4}$$

where $W_{ij} = W(\boldsymbol{x}_i - \boldsymbol{x}_j, h)$.

Viscosity forces, representing internal friction within the fluid, are computed as:

$$\nu \nabla^2 \boldsymbol{v}_i = \nu \sum_j m_j \left(\frac{\boldsymbol{v}_{ij} \cdot \boldsymbol{x}_{ij}}{|\boldsymbol{x}_{ij}|^2 + \epsilon^2}\right) \nabla W_{ij}, \tag{5}$$

where $\epsilon = 0.01h^2$ ϵ being a small value added to prevent singularity when particles are very close. $\boldsymbol{v}_{ij} = \boldsymbol{v}_i - \boldsymbol{v}_j$ and $\boldsymbol{x}_{ij} = \boldsymbol{x}_i - \boldsymbol{x}_j$ represent the relative velocity and position.

4 Dual-Mechanism Surface Tension Model

In this section, we delve into the intricate details of our dual-mechanism surface tension model, which stands out for its innovative approach to simulating fluid dynamics with enhanced precision and stability.

4.1 Surface Particle Detection and Correction

A crucial component of our model is the precise identification and subsequent correction of surface particles, essential for preserving the accuracy of fluid simulations, particularly in regions near free surfaces or

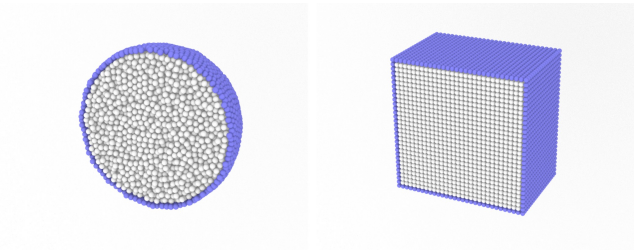

Fig. 3: Spherical and cubic surface detection. Surface particles and interior particles are shown in blue and white respectively. ($\eta = 0.88$)

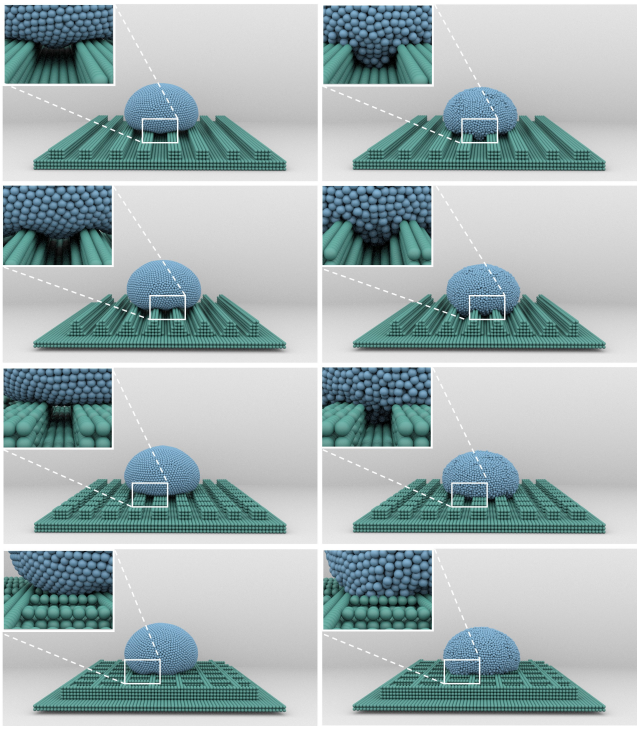

Fig. 4: Superhydrophobic effect on rough surface. We set the droplet to fall on four types of surfaces: rectangular, sinusoidal, dual-rectangular and dual-sinusoidal. In the Cassie state, we can observe light passing through the gap; in the Wenzel state, droplet sinks into the grooves.

phase interfaces where the distribution of particles is less dense. In such scenarios, conventional SPH methods might not accurately maintain the simulation's integrity, potentially leading to inaccuracies in the depiction of fluid dynamics and interactions. Specifically, at the interface or free surface, the diminished value of $\psi(\boldsymbol{x})$ in Eq. (2) becomes insufficient due to the truncation of the smoothing kernel, as illustrated in Fig.2. This necessitates an independent correction for these particles.

In our surface tension model, updating particle labels at each timestep is essential to accurately apply distinct algorithms for interior and surface particles. This necessitates a reliable and efficient technique for classifying particles. To achieve this, we utilize an advanced interpolation function inspired by Shepard's method [26], which effectively distinguishes between surface and interior particles. This approach computes a discriminant value D_i for each particle, employing a distance-weighted sum. For the weighting function, we select the Wendland kernel [30] due to it is a compactly supported function, which contribute to the robustness and efficiency of our surface detection process:

$$D_i = \begin{cases} \sum_j^N \boldsymbol{d}_{ij}\xi_{ij} / \sum_j^N \boldsymbol{d}_{ij} & \boldsymbol{d}_{ij} \neq 0 \\ \xi_{ij} & \boldsymbol{d}_{ij} = 0 \end{cases}, \tag{6}$$

where $\boldsymbol{d}_{ij}$ is the Cartesian distance. The term $\xi_{ij} = \frac{m_j}{\rho_j}$, where m_j is the mass and ρ_j is the density of particle j. Eq.(6) is refined as $D_i = \sum_j^N \xi_{ij} W_{ij}$. The value of D_i can be used to differentiate interior particles from surface particles by introducing a threshold η ($\eta < 1$). If $D_i > \eta$, particle i is defined as an interior particle; otherwise, it is categorized as a surface particle. The result of surface particle detection is shown in Fig. 3. We replace $\boldsymbol{d}_{ij}$ with a distance weighting factor derived from the Wendland kernel [30], defined by:

$$W_{ij} = \begin{cases} \frac{21}{16\pi h^3}\left(1 - \frac{\boldsymbol{x}_{ij}}{2h}\right)^4 \left(\frac{2\boldsymbol{x}_{ij}}{h} + 1\right) & \boldsymbol{x}_{ij} \leq h \\ 0 & \boldsymbol{x}_{ij} > h \end{cases}. \tag{7}$$

Here, $\boldsymbol{x}_{ij} = \boldsymbol{x}_i - \boldsymbol{x}_j$ represents the distance between particles i and j, and h is the smoothing length. This kernel smoothly diminishes with distance, ensuring contributions from neighboring particles decrease as they move further away.

For surface particles, the kernel encompasses both gas and fluid particles, necessitating a division into inside area Ω_i and outside area Ω_o at the phase boundary, illustrated in Fig. 2. The pressure force for surface particles is then adjusted to account for external gas pressure, comprising environmental pressure (p_{env}) and the Laplace pressure jump (Δp) at curved gas-liquid interfaces. The modified pressure force equation is:

$$\begin{aligned} -\frac{1}{\rho_i}\nabla p_i = &-\sum_{\Omega_i} m_j \left(\frac{p_i}{\rho_i^2} + \frac{p_j}{\rho_j^2}\right)\nabla W_{ij} \\ &-\sum_{\Omega_o} m_j \left(\frac{p_i}{\rho_i^2} + \frac{\Delta p + p_{\text{env}}}{\rho_j^2}\right)\nabla W_{ij}. \end{aligned} \tag{8}$$

For interior particles, where p_{env} and Δp effectively become zero and contributions from particles in Ω_o are not considered, the pressure force calculation reverts to the symmetric form as per the standard SPH methodology. This distinction in pressure force calculation for surface versus interior particles enhances the accuracy and stability of simulations, especially in capturing the dynamics at fluid interfaces and free surfaces.

4.2 Laplace Pressure Jump

The Laplace pressure jump (Δp), incorporated in Eq. (8), plays a crucial role in our surface tension model, especially noticeable at sharp free surfaces. This pressure

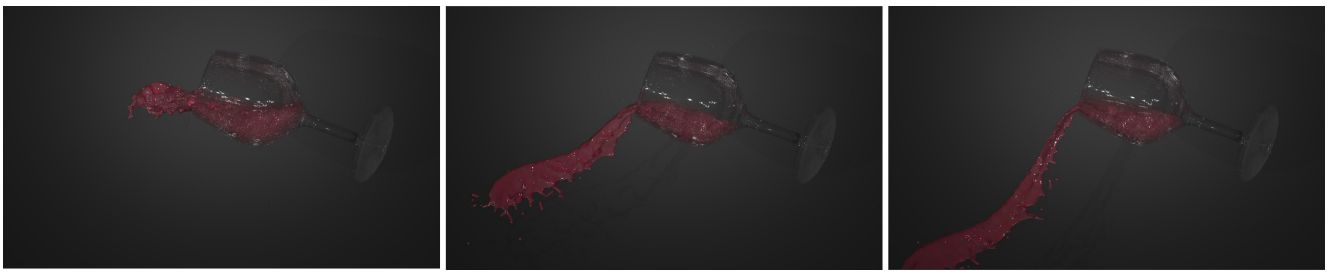

Fig. 5: Stream-ribbon of wine.

differential is attributed to surface tension forces and is quantitatively determined by the curvature of the fluid surface, as articulated by the Young-Laplace equation:

$$\Delta p = -\gamma \nabla \cdot \boldsymbol{n} = 2\gamma H = \gamma \left(\frac{1}{R_1} + \frac{1}{R_2} \right), \tag{9}$$

where γ represents the surface tension coefficient, $\hat{\boldsymbol{n}}$ denotes the normalized normal vector to the surface, and H signifies the mean curvature with R_1 and R_2 being the principal curvature radii of the surface.

To compute the normal vector $\boldsymbol{n}_i$ at the surface, we employ the following formulation:

$$\boldsymbol{n}_i = -\frac{1}{D_i} \sum_j \frac{m_j^2}{\rho_j^2} W_{ij} \sum_j \nabla W_{ij}, \tag{10}$$

where W_{ij} is the smoothing kernel function as defined in Eq. (7), and D_i is the discriminant value used to differentiate surface particles, ensuring that the calculation accounts for the truncated kernel effect. This approach, through the factor $\frac{1}{D_i}$, scales the normal vector computation for surface particles, effectively mitigating the noise typically encountered in surface normal calculations. The normalized form of the normal vector is expressed as $\hat{\boldsymbol{n}}_i$, which is essential for accurately determining the curvature and, consequently, the Laplace pressure jump across the fluid interface. Our experimental results validate the efficacy of this method in enhancing the precision of surface-related computations within the SPH framework.

To enhance the precision of gradient interpolation within our model, we incorporate a renormalization technique inspired by Oger *et al.* [23], which adjusts the gradient of the kernel function ∇W. This adjustment is crucial for maintaining the accuracy of calculated gradients, particularly in the context of surface tension modeling where precise curvature measurements are essential. The renormalized kernel gradient $\nabla^R W$ is defined as:

$$\nabla^R W\left(\boldsymbol{x}_i - \boldsymbol{x}_j\right) = R(x)^{-1} \nabla W\left(\boldsymbol{x}_i - \boldsymbol{x}_j\right), \tag{11}$$

where $R(\boldsymbol{x})$ is a correction matrix of dimension $d \times d$, with d representing the spatial dimensionality of the problem. This matrix corrects the gradient based on the spatial configuration of neighboring particles, ensuring that the interpolation of gradients remains consistent even in complex flow scenarios.

For illustrative purposes, the two-dimensional form of the correction matrix $R(\boldsymbol{x})$ is presented, showcasing how the matrix elements are computed based on the spatial differences between particle positions and the gradients of the smoothing kernel weighted by ω_j, which represents the volume equivalent of particle j:

$$\begin{pmatrix} \sum\limits_j^N \left(\boldsymbol{x}_j^1 - \boldsymbol{x}_i^1\right) \nabla W\left(\boldsymbol{x}_{ij}\right) \omega_j & \sum\limits_j^N \left(\boldsymbol{x}_j^1 - \boldsymbol{x}_i^1\right) \nabla W\left(\boldsymbol{x}_{ij}\right) \omega_j \\ \sum\limits_j^N \left(\boldsymbol{x}_j^2 - \boldsymbol{x}_i^2\right) \nabla W\left(\boldsymbol{x}_{ij}\right) \omega_j & \sum\limits_j^N \left(\boldsymbol{x}_j^2 - \boldsymbol{x}_i^2\right) \nabla W\left(\boldsymbol{x}_{ij}\right) \omega_j \end{pmatrix}. \tag{12}$$

The curvature tensor $\boldsymbol{K}_i$, a pivotal component in calculating surface curvature and, by extension, the Laplace pressure jump, is derived using this renormalized kernel gradient:

$$\boldsymbol{K}_i = \sum_j^N \omega_j \hat{\boldsymbol{n}}_{ij} \otimes \nabla^R W_{ij}, \tag{13}$$

where $\hat{\boldsymbol{n}}_{ij}$ is the difference in normalized normal vectors between particles i and j.

To calculate the mean curvature as referenced in Eq. (9), we need to determine the principal curvature radii. Drawing from shell theory in solid mechanics [24] and adapting for our fluid simulation context, we establish a local coordinate system using normalized orthogonal tangent vectors and the normal vector from Eq. (10). The basis vectors for this system are $\boldsymbol{L} = \left(\hat{\boldsymbol{n}}_i, \hat{\boldsymbol{t}}_i^1, \hat{\boldsymbol{t}}_i^2\right)$. The first tangent vector $\boldsymbol{t}_i^1$ is computed as follows:

$$\boldsymbol{t}_i^1 = \begin{cases} \hat{\boldsymbol{n}}_i \times (0,1,0) & \text{if } \|\hat{\boldsymbol{n}}_i \times (0,1,0)\| > 0.01 \\ \hat{\boldsymbol{n}}_i \times (1,0,0) & \text{else} \end{cases}, \tag{14}$$

to ensure orthogonality with $\hat{\boldsymbol{n}}_i$.

The second tangent vector $\boldsymbol{t}_i^2$ is obtained via the cross product $\boldsymbol{t}_i^2 = \hat{\boldsymbol{n}}_i \times \hat{\boldsymbol{t}}_i^1$, ensuring a mutually orthogonal set of vectors. The curvature tensor $\boldsymbol{K}_i$ in Eq. (13)

is then transformed from the Cartesian to the local coordinate system using the transformation matrix $\boldsymbol{T}_i$, as defined by:

$$\widetilde{\boldsymbol{K}}_i = \boldsymbol{T}_i^{\mathrm{T}} \boldsymbol{K}_i \boldsymbol{T}_i, \tag{15}$$

where $\boldsymbol{T}_i$ aligns the curvature tensor with the local coordinate system established by $\boldsymbol{L}$. This transformation facilitates the accurate calculation of curvature by considering the local geometry of the fluid surface.

To deduce the principal curvatures $\frac{1}{R_1}$ and $\frac{1}{R_2}$, we evaluate the eigenvalues of the transformed curvature tensor $\widetilde{\boldsymbol{K}}_i$, which has been adjusted to a 2D form by omitting components along the normal direction. The Laplace pressure jump Δp_i is then adjusted to account for these curvatures, enhancing the model's stability and accuracy in simulating surface tension effects:

$$\Delta p_i = \frac{\gamma_i}{2} \left(\frac{1}{R_{1\,i}} + \frac{1}{R_{2\,i}} \right) \left(\frac{1}{D_i} + 1 \right). \tag{16}$$

4.3 Combined Surface Tension Force

Our model introduces a nuanced approach to the computation of surface tension forces by incorporating a dual-scale smoothing kernel. This method addresses the limitations identified in previous studies, such as those by Yang *et al.* [33], who utilized a larger smoothing kernel to enhance the stability of surface tension effects but at the cost of losing fine details due to the expanded neighbor search radius. Directly reducing the kernel size could lead to inaccuracies from insufficient neighbor particles. To mitigate these issues, we propose an interaction force that leverages both the standard and a reduced-scale smoothing kernel, as described by:

$$\boldsymbol{F}_i^{\text{interaction}} = \sum_j^N \left(a_{ij} W\left(\boldsymbol{x}_{ij}, h\right) - b_{ij} W\left(\boldsymbol{x}_{ij}, 0.7h\right) \right) \frac{\boldsymbol{x}_{ij}}{|\boldsymbol{x}_{ij}|}, \tag{17}$$

where W is defined as $\cos\left(\frac{3\pi}{2h}\left|\boldsymbol{x}_{ij}\right|\right)$, with a_{ij} and b_{ij} representing coefficients for the standard and reduced-scale kernels, respectively. This dual-scale approach allows for the preservation of detail while maintaining the stability improvements seen with larger kernels.

To illustrate the effectiveness of this approach, we simulate the behavior of droplets on various textured surfaces, modeling superhydrophobic phenomena as described by Cassie [6] and Wenzel [31]. In the Cassie state, droplets are supported above the surface by micro- or nano-structures, creating air pockets beneath them, whereas in the Wenzel state, the liquid fully wets the textured surface, filling the grooves. These distinct behaviors are crucial for understanding and simulating superhydrophobic surfaces, and our model's capability to accurately represent both states is demonstrated in Fig. 4, showcasing the versatility and precision of our dual-scale kernel method in capturing complex surface interactions.

To accurately represent the intricate behaviors of fluids interacting with textured surfaces, such as those depicted in Fig. 4, we employ a mathematical model to construct sinusoidal and dual-sinusoidal surfaces. The height function for these surfaces is defined as:

$$h(x) = \frac{A}{2} \sin\left(\frac{2\pi x}{T}\right) + 0.05 \tag{18}$$

where $A = 0.3$ and $T = 0.5$ denote the amplitude and period of the sinusoidal wave, respectively, and h represents the height of the surface features.

While the interaction force, defined by Eq. 17, is adept at simulating fluid behaviors on both smooth and textured surfaces, it does not inherently ensure the minimization of surface area, a fundamental characteristic of surface tension.

Additionally, early stages of the simulation may exhibit perturbations in kinetic energy, a challenge commonly encountered with IIF methods. To address these issues, we introduce a curvature force component, computed using the principal curvature radii determined in Section 4.2, as follows:

$$\boldsymbol{F}_i^{curvature} = \gamma_i \boldsymbol{n}_i \left(\frac{1}{R_{1\,i}} + \frac{1}{R_{2\,i}} \right). \tag{19}$$

This force component is nullified for particles on flat surfaces by making Eq. (19) equal to zero, where the curvature radii are infinite, and is progressively amplified for particles on more curved surfaces. Fig. 6, illustrating the model's capability to accurately replicate the behavior of fluids under the influence of surface tension.

The overall surface tension force $\boldsymbol{F}_i^{ST}$ in Eq. (1) for each particle is computed by combining the interaction force $\boldsymbol{F}_i^{interaction}$ with the curvature force $\boldsymbol{F}_i^{curvature}$, as integrated within the Weakly Compressible SPH (WCSPH) framework. This comprehensive approach, detailed in our algorithm (Algorithm 1), allows for the simulation of complex fluid dynamics, ensuring realistic depiction of surface tension phenomena in fluid simulations.

5 Experiments

We implement the algorithm by using Taichi [13] and Python programming language on the Nvidia GeForce

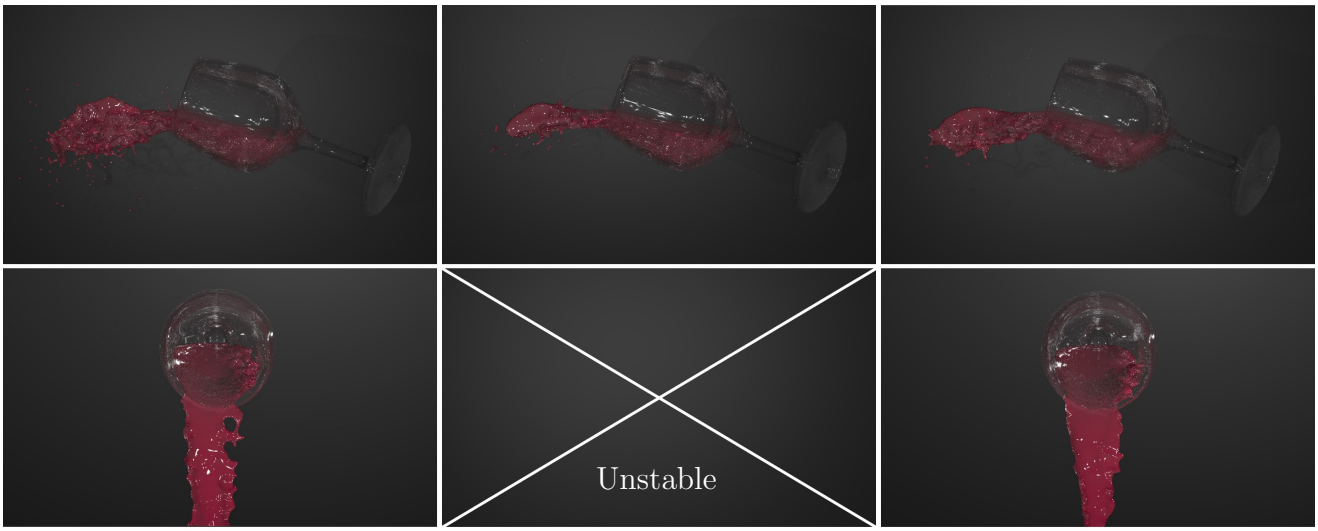

Yang *et al.* [33] (a) | Yang *et al.* [33] (b) | Our Method (c)

Fig. 6: Comparison of surface area minimization. We compare our method with Yang *et al.* [33] in same frame. Fig.(c) significantly reduces particle splashing compared to Fig.(a) by minimizing the surface area under the same scale of surface tension We attempted to address this issue by enhancing the surface tension; yet, it led to an unstable simulation outcome in Fig.(b).

Fig. 7: Dew on the palm leaf.

RTX 4060 GPU. We conducted the following experiments to demonstrate the effectiveness and superiority of our method. Surface reconstruction and rendering are performed using the Mantra engine in Houdini. The performance for all examples are summarized in Table 1.

Table 1: Efficiency Performance on Examples

Examples	**Particles**	**Steps/ Frame**	**Msec/ Frame**	**Frames/ Frame**
Oscillation	43K	8	14.4	69.4
Stream-ribbon	82K	8	16.8	59.5
Bubble	23K	10	11.8	84.7
Rough surface	12K	5	12.5	80.0
Palm leaf	2K	10	9.1	109.9

Droplet oscillation In the absence of gravitational forces, Fig. 8 illustrates the evolution of a cubic droplet undergoing oscillations driven by surface tension, eventually adopting a spherical shape. This transformation is characterized by setting $\gamma = 100$ and the coefficient $a = 30$. As a benchmark for evaluating surface tension models, the kinetic energy associated with the droplet's oscillation is plotted against time steps, depicted in Fig. 9, serving as an indicator of our model's capability to accurately incorporate Laplace pressure adjustments.

Fig. 9(a) focuses on the impact of Laplace pressure in the context of CSF methods, where surface tension is solely accounted for by curvature forces. Here, the kinetic energy exhibits a gradual decline, punctuated by clear, periodic oscillations corresponding to the cubic droplet's deformation, highlighted by the green line in the graph.

Subsequently, Fig. 9(b) juxtaposes our method against that of Yang *et al.* [33], offering a comparative anal-

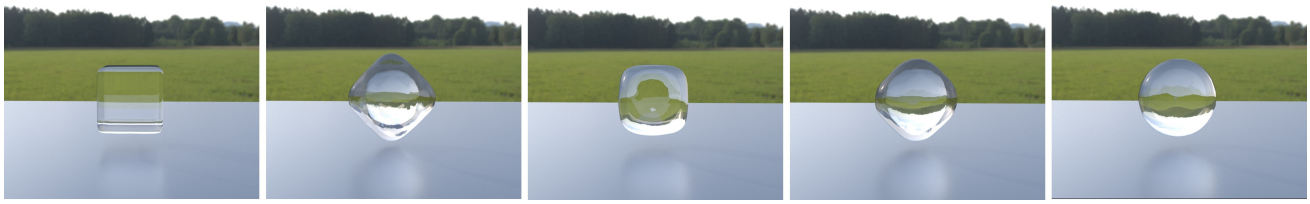

Fig. 8: Droplet oscillation in zero-gravity.

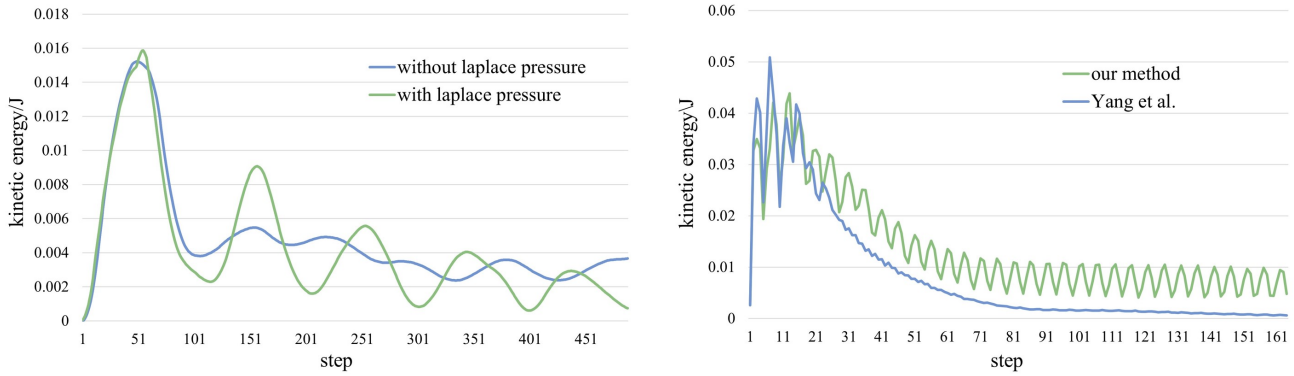

(a) Comparison of Laplace pressure on CSF methods. (b) Comparison of our method and Yang *et al.* [33] method.

Fig. 9: Kinetic energy of droplet oscillation as a function of time step.

Algorithm 1 Simulation Loop

Preparation
- search neighboring particles
- update density ρ_i
- calculate viscosity force and gravity (5)

Detection
- update detection value D_i (6)
- compute pressure force for interior particles (4)

Surface Tension
- compute $\boldsymbol{F}_i^{\text{interaction}}$ (17)
- update normal vector (10)
- normalized kernel gradient $\nabla^R W$ (11)
- compute curvature tensor $\boldsymbol{K}_i$ (13)
- compute principal curvature radius R_1, R_2 from $\widetilde{\boldsymbol{K}}_i$ (15)
- compute curvature force $\boldsymbol{F}_i^{curvature}$ (19)

Pressure Correction
- update Laplace pressure Δp_i (16)
- correct pressure force for surface particle (8)
- update velocity and position

ysis. Unlike our model, Yang et al.'s approach does not capture distinct oscillatory behavior, and an unexplained disturbance is noticeable in the early simulation stages, underscoring the advantages of our enhanced surface tension treatment.

Stream-ribbon This experiment simulates a scenario where red wine is poured from a tilted glass, creating a stream-ribbon of wine flowing through the air, as depicted in Fig. 5. We adjusted the tension coefficient γ to 40 to observe the effects on the fluid's surface tension. The results on the left side of the figure demonstrate a noticeably smoother flow, indicating that our surface tension model effectively minimizes the fluid surface area. From a frontal perspective, our approach successfully preserves the integrity of the thin film structure, preventing any discontinuities. This experiment underscores the ability of our method to accurately represent slender fluid features and highlights the enhanced stability of our surface tension model in handling delicate fluid dynamics.

Bubble coalescence Our model adeptly simulates bubble dynamics by robustly handling the gas-liquid interface via Laplace pressure adjustments. Within this setup, the bubble's film is composed of fluid particles, while the interior is filled with gas particles. Initially, two bubbles of differing sizes are placed at a distance from each other. Driven by inter-particle forces, they gradually move towards one another, culminating in a coalescence event as illustrated in Figure 1. The parameters set for this simulation were $\gamma = 100$, with coefficients $a = 100$ and $b = 10$, respectively, showcasing our model's capability to simulate complex bubble interactions.

Superhydrophobic surface Fig. 4 showcases four distinct rough surfaces characterized by pronounced protrusions and indentations, designed to mimic superhydrophobic

textures at the microscale. These surfaces serve as a basis for simulating the superhydrophobic effect, successfully capturing both Cassie and Wenzel wetting states. The employment of a dual-scale smoothing kernel allows for a detailed depiction of droplets interacting with surface grooves. The simulation parameters for the Cassie state were set to $a = 130$ and $b = 10$, while for the Wenzel state, they were adjusted to $a = 130$ and $b = 120$, facilitating the accurate representation of these complex wetting phenomena.

Dew on the palm leaf This scenario visualizes a droplet landing on a palm leaf, emulating the behavior of dew being enveloped by an elastic membrane. The simulation captures the droplet's stable slide across the leaf's surface and its eventual detachment upon reaching a wider gap. This setup highlights our model's proficiency in managing fluid interactions with discontinuous surfaces and intricate boundaries, providing a realistic portrayal of dew accumulation and movement on foliage. The simulation parameters were set to $a = 130$, $b = 20$, and $\gamma = 10$, demonstrating the model's effectiveness in rendering detailed fluid-surface interactions.

6 Conclusion and Discussion

In this work, we have introduced a new dual-mechanism model for simulating surface tension, effectively combining particle interaction forces with curvature forces. This integration allows for the accurate depiction of a wide range of behaviors, while also maintaining surface stability and minimizing surface area. Our method overcomes common issues related to curvature computation inaccuracies by categorizing particles as either surface or interior types, and it addresses the truncated kernel problem at fluid interfaces through the application of Laplace pressure corrections.

Our model's stability and efficacy have been thoroughly evaluated, both numerically and visually, demonstrating significant improvements over existing techniques. Additionally, we have expanded the realm of surface tension simulations to include interactions with specially textured rough surfaces, an aspect often overlooked in previous research. The implementation of a dual-scale smoothing kernel in our model recovers critical surface details, enabling the simulation of superhydrophobic phenomena, which represents a novel contribution to the field.

Despite these advancements, our current model employs an explicit approach for calculating Laplace pressure, which may restrict the time step size in large-scale simulations. Future work will explore implicit formulations of Laplace pressure that can be seamlessly integrated with implicit pressure solvers, enhancing the model's scalability and applicability. Moreover, we aim to extend our investigation into the interactions between fluids and porous materials, delving into phenomena such as fluid penetration and absorption, to further enrich the capabilities and realism of our surface tension model.

References

1. Akinci, N., Akinci, G., Teschner, M.: Versatile surface tension and adhesion for sph fluids. ACM Transactions on Graphics (TOG) **32**(6), 1–8 (2013)
2. Batty, C., Uribe, A., Audoly, B., Grinspun, E.: Discrete viscous sheets. ACM Transactions on Graphics (TOG) **31**(4), 1–7 (2012)
3. Becker, M., Teschner, M.: Weakly compressible sph for free surface flows. In: Acm Siggraph/eurographics Symposium on Computer Animation (2007)
4. Bergou, M., Audoly, B., Vouga, E., Wardetzky, M., Grinspun, E.: Discrete viscous threads. ACM Transactions on graphics (TOG) **29**(4), 1–10 (2010)
5. Brackbill, J.U., Kothe, D.B., Zemach, C.: A continuum method for modeling surface tension. Journal of computational physics **100**(2), 335–354 (1992)
6. Cassie, A., Baxter, S.: Wettability of porous surfaces. Transactions of the Faraday society **40**, 546–551 (1944)
7. Chen, J., Kala, V., Marquez-Razon, A., Gueidon, E., Hyde, D.A., Teran, J.: A momentum-conserving implicit material point method for surface tension with contact angles and spatial gradients. ACM Transactions on Graphics (TOG) **40**(4), 1–16 (2021)
8. Chen, Y.L., Meier, J., Solenthaler, B., Azevedo, V.C.: An extended cut-cell method for sub-grid liquids tracking with surface tension. ACM Transactions on Graphics (TOG) **39**(6), 1–13 (2020)
9. Clavet, S., Beaudoin, P., Poulin, P.: Particle-based viscoelastic fluid simulation. In: Proceedings of the 2005 ACM SIGGRAPH/Eurographics symposium on Computer animation, pp. 219–228 (2005)
10. Da, F., Batty, C., Wojtan, C., Grinspun, E.: Double bubbles sans toil and trouble: Discrete circulation-preserving vortex sheets for soap films and foams. ACM Transactions on Graphics (TOG) **34**(4), 1–9 (2015)
11. Da, F., Hahn, D., Batty, C., Wojtan, C., Grinspun, E.: Surface-only liquids. ACM Transactions on Graphics (TOG) **35**(4), 1–12 (2016)
12. He, X., Wang, H., Zhang, F., Wang, H., Wang, G., Zhou, K.: Robust simulation of sparsely sampled thin features in sph-based free surface flows. ACM Transactions on Graphics (TOG) **34**(1), 1–9 (2014)
13. Hu, Y., Li, T.M., Anderson, L., Ragan-Kelley, J., Durand, F.: Taichi: a language for high-performance computation on spatially sparse data structures. ACM Transactions on Graphics (TOG) **38**(6), 201 (2019)
14. Huber, M., Reinhardt, S., Weiskopf, D., Eberhardt, B.: Evaluation of surface tension models for sph-based fluid animations using a benchmark test. In: VRIPHYS, pp. 41–50 (2015)
15. Hyde, D.A., Gagniere, S.W., Marquez-Razon, A., Teran, J.: An implicit updated lagrangian formulation for liquids with large surface energy. ACM Transactions on Graphics (TOG) **39**(6), 1–13 (2020)

16. Ihmsen, M., Cornelis, J., Solenthaler, B., Horvath, C., Teschner, M.: Implicit incompressible sph. IEEE Transactions on Visualization & Computer Graphics **20**(3), 426–435 (2014)
17. Ishida, S., Synak, P., Narita, F., Hachisuka, T., Wojtan, C.: A model for soap film dynamics with evolving thickness. ACM Transactions on Graphics (TOG) **39**(4), 31–1 (2020)
18. Ishida, S., Yamamoto, M., Ando, R., Hachisuka, T.: A hyperbolic geometric flow for evolving films and foams. ACM Transactions on Graphics (TOG) **36**(6), 1–11 (2017)
19. Jeske, S.R., Westhofen, L., Löschner, F., Fernández-fernández, J.A., Bender, J.: Implicit surface tension for sph fluid simulation. ACM Transactions on Graphics **43**(1), 1–14 (2023)
20. Monaghan, J.J.: Simulating free surface flows with sph. Journal of computational physics **110**(2), 399–406 (1994)
21. Morris, J.P.: Simulating surface tension with smoothed particle hydrodynamics. International journal for numerical methods in fluids **33**(3), 333–353 (2000)
22. Müller, M., Charypar, D., Gross, M.: Particle-based fluid simulation for interactive applications. In: Proceedings of the 2003 ACM SIGGRAPH/Eurographics symposium on Computer animation, pp. 154–159 (2003)
23. Oger, G., Doring, M., Alessandrini, B., Ferrant, P.: An improved sph method: Towards higher order convergence. Journal of Computational Physics **225**(2), 1472–1492 (2007)
24. Plateau, J.A.F.: Statique expérimentale et théorique des liquides soumis aux seules forces moléculaires, vol. 2. Gauthier-Villars (1873)
25. Ruan, L., Liu, J., Zhu, B., Sueda, S., Wang, B., Chen, B.: Solid-fluid interaction with surface-tension-dominant contact. ACM Transactions on Graphics (TOG) **40**(4), 1–12 (2021)
26. Shepard, D.: A two-dimensional interpolation function for irregularly-spaced data. In: Proceedings of the 1968 23rd ACM national conference, pp. 517–524 (1968)
27. Wang, H., Jin, Y., Luo, A., Yang, X., Zhu, B.: Codimensional surface tension flow using moving-least-squares particles. ACM Transactions on Graphics (TOG) **39**(4), 42–1 (2020)
28. Wang, M., Deng, Y., Kong, X., Prasad, A.H., Xiong, S., Zhu, B.: Thin-film smoothed particle hydrodynamics fluid. ACM Transactions on Graphics (TOG) **40**(4), 1–16 (2021)
29. Wang, X.K., Ban, X.J., Zhang, Y.L., Liu, S.N., Ye, P.F.: Surface tension model based on implicit incompressible smoothed particle hydrodynamics for fluid simulation. Journal of Computer Science and Technology **32**, 1186–1197 (2017)
30. Wendland, H.: Piecewise polynomial, positive definite and compactly supported radial functions of minimal degree. Advances in computational Mathematics **4**, 389–396 (1995)
31. Wenzel, R.N.: Resistance of solid surfaces to wetting by water. Industrial & engineering chemistry **28**(8), 988–994 (1936)
32. Xing, J., Ruan, L., Wang, B., Zhu, B., Chen, B.: Position-based surface tension flow. ACM Transactions on Graphics (TOG) **41**(6), 1–12 (2022)
33. Yang, T., Lin, M., Martin, R.R., Chang, J., Hu, S.: Versatile interactions at interfaces for sph-based simulations. In: Eurographics/ACM SIGGRAPH Symposium on Computer Animation (2016), pp. 57–66. Association for Computing Machinery (2016)
34. Yang, T., Martin, R.R., Lin, M.C., Chang, J., Hu, S.M.: Pairwise force sph model for real-time multi-interaction applications. IEEE transactions on visualization and computer graphics **23**(10), 2235–2247 (2017)
35. Zhang, M.: Simulation of surface tension in 2d and 3d with smoothed particle hydrodynamics method. Journal of Computational Physics **229**(19), 7238–7259 (2010)
36. Zhang, Y., Wang, H., Wang, S., Tong, Y., Zhou, K.: A deformable surface model for real-time water drop animation. IEEE Transactions on Visualization and Computer graphics **18**(8), 1281–1289 (2011)
37. Zhu, B., Quigley, E., Cong, M., Solomon, J., Fedkiw, R.: Codimensional surface tension flow on simplicial complexes. ACM Transactions on Graphics (TOG) **33**(4), 1–11 (2014)
38. Zorilla, F., Ritter, M., Sappl, J., Rauch, W., Harders, M.: Accelerating surface tension calculation in sph via particle classification and monte carlo integration. Computers **9**(2), 23 (2020)